nature energy

Article

https://doi.org/10.1038/s41560-025-01817-6

Cation interdiffusion control for 2D/3D heterostructure formation and stabilization in inorganic perovskite solar modules

Received: 17 December 2023

Accepted: 17 June 2025

Published online: 16 July 2025

Check for updates

Cheng Liu[1,2], Yi Yang[1,2], Jared D. Fletcher[1], Ao Liu[1], Isaiah W. Gilley[1], Charles Bruce Musgrave III[1], Zaiwei Wang[3], Huihui Zhu[1], Hao Chen[1], Robert P. Reynolds[1], Bin Ding[2], Yong Ding[2], Xianfu Zhang[1,2], Raminta Skackauskaite[4], Haoyue Wan[1,3], Lewei Zeng[3], Abdulaziz S. R. Bati[1], Naoyuki Shibayama[5], Vytautas Getautis[4], Bin Chen[1], Kasparas Rakstys[4] ✉, Paul J. Dyson[2] ✉, Mercouri G. Kanatzidis[1] ✉, Edward H. Sargent[1,3,6] ✉ & Mohammad K. Nazeeruddin[2,7] ✉

Inorganic perovskite solar cells could benefit from surface passivation using 2D/3D perovskite heterostructures. However, conventional spacer cations fail to exchange with the tightly bonded Cs cation in the inorganic perovskite to form 2D layers atop; or, when they do enable formation of a 2D layer, they migrate under heat, degrading device performance. Here we investigate the mechanisms behind 2D/3D heterostructure formation and stabilization. We find that 2D/3D heterostructure formation is driven by interactions between ammonium groups and $[PbI_6]^{4-}$ octahedra. We thus incorporate electron-withdrawing fluorine to enhance inorganic–organic cation interdiffusion and promote heterostructure formation. We note that stability relies on interactions between the entire spacer cations and $[PbI_6]^{4-}$ octahedra. We therefore introduce anchoring groups that double cation desorption energies, preventing cation migration at elevated temperatures. $CsPbI_3$/(perfluoro-1,4-phenylene)dimethanammonium lead iodide heterostructures enable an efficiency of 21.6% and a maximum power point operating stability at 85 °C of 950 h. We demonstrate 16-cm^2 modules with an efficiency of 19.8%.

Inorganic perovskites, with restricted ion migration and high decomposition temperatures, have emerged as promising photovoltaic materials, offering increased photo and thermal stability compared to their organic–inorganic hybrid counterparts[1–6]. Single-junction perovskite solar cells (PSCs) utilizing inorganic perovskites as the active layer have achieved power conversion efficiencies (PCEs) exceeding 21% on small areas (<0.1 cm^2) (refs. 7–10) and up to 26% when incorporated into tandem solar cells[11–13].

However, surface defects generated on the film during high-temperature solution processing of inorganic perovskites result in non-radiative charge recombination at device interfaces, limiting the PCE to levels far from the Shockley–Queisser theoretical value[14–17]. Additionally, the imperfect Goldschmidt tolerance factor contributes to decreased phase stability in inorganic perovskites, particularly under humid conditions[18–20].

To address these issues, surface passivation with two-dimensional (2D) perovskites and their organic ligands has been developed to reduce surface defects and enhance long-term stability in inorganic PSCs[21–25]. However, conventional spacer cations either fail to form 2D layers atop inorganic 3D perovskite—probably due to the strong ionic

A full list of affiliations appears at the end of the paper. ✉e-mail: kasparas.rakstys@ktu.lt; paul.dyson@epfl.ch; m-kanatzidis@northwestern.edu; ted.sargent@northwestern.edu; mdkhaja.nazeeruddin@epfl.ch

https://doi.org/10.1038/s41560-025-01817-6

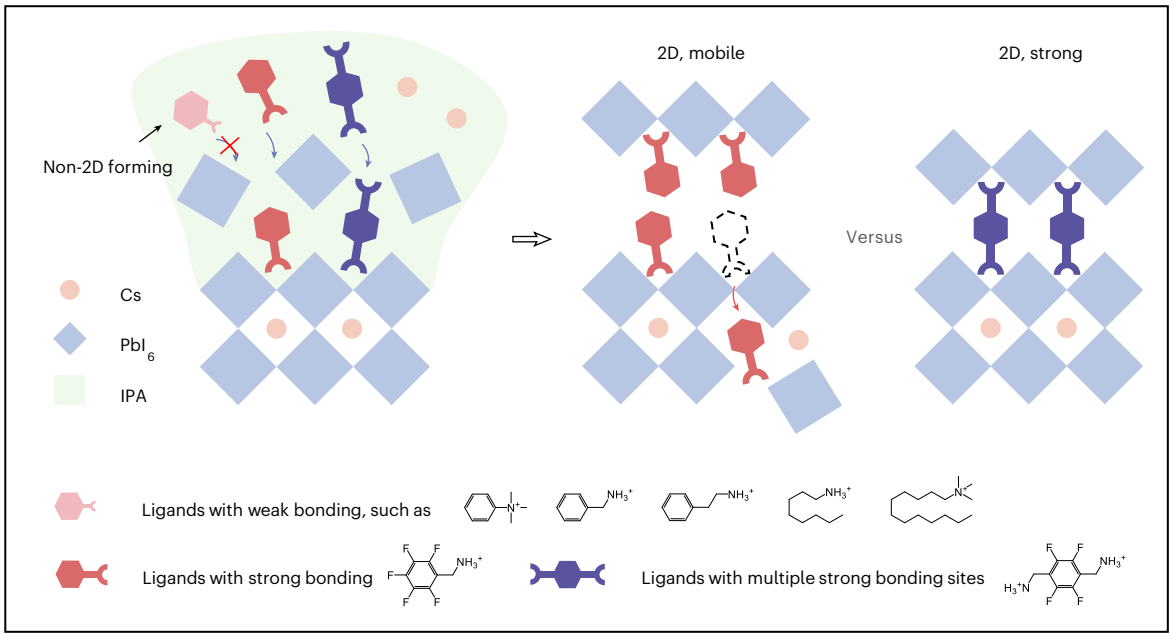

Fig. 1 | Formation, degradation and stabilization of 2D/3D perovskite heterostructures. Ligands with weak bonding are unable to form 2D layers atop inorganic 3D perovskites[14,24,30,31]. Ligands with strong bonding can form 2D/3D heterostructures, but only ligands with multiple strong bonding sites can form and stabilize these 2D/3D heterostructures. IPA, isopropanol.

lattice formed by Cs^+ and $[PbI_6]^{4-}$ octahedra, which hinders the accommodation of bulky organic layers[5,11,24]; or they migrate, particularly under elevated temperature, resulting in heterostructure collapse, loss of interfacial passivation and accelerated device degradation[26–29]. These issues—either the inability to form 2D layers or the instability of the formed layers—are particularly problematic given the phase instability of inorganic perovskites under external stresses. The formation and stabilization mechanisms of 2D/3D heterostructures until now have been underexplored in the inorganic perovskite field. A comprehensive design of cation structures should be investigated to uncover these mechanisms and address these challenges, thereby contributing to the construction of a robust heterojunction for achieving efficient and stable inorganic PSCs.

In this study, we posit that the interaction between spacer cations and $[PbI_6]^{4-}$ is crucial for the formation and stabilization of the 2D/3D heterostructure[14,24,30,31] (Fig. 1). We explored a set of spacer cations with varying functional groups and found that the formation of these heterostructures is driven by the interaction between ammonium groups and $[PbI_6]^{4-}$ octahedra; whereas their stabilization hinges on the interactions between spacer cations and $[PbI_6]^{4-}$ octahedra. Building on this understanding, we studied cations bearing electron-withdrawing fluorine atoms at the molecular tail to strengthen the ammonium–$[PbI_6]^{4-}$ interactions and promote interdiffusion between inorganic cations and organic spacers, facilitating the formation of 2D/3D heterostructures. In parallel, incorporating extra anchoring groups enhanced spacer cation–$[PbI_6]^{4-}$ interactions, doubling the cation desorption energy and stabilizing the heterostructures against cation migration under elevated temperatures. As a result, we identified $CsPbI_3$/(perfluoro-1,4-phenylene)dimethanammonium lead iodide heterostructures that enable a PSC efficiency of 21.6% with MPP operational stability of 950 h at 85 °C. Furthermore, perovskite solar modules measuring 16 cm^2 achieved an efficiency of 19.8%.

Construction of 2D/3D perovskite heterostructures

We began by screening spacer cations based on two principles: (1) incorporating electron-withdrawing fluorine into tail groups should enhance the interactions between ammonium groups and $[PbI_6]^{4-}$ octahedra[32]; (2) adding additional anchoring groups, such as Dion–Jacobson cations, should strengthen the overall interaction between spacer cations and $[PbI_6]^{4-}$ octahedra[33].

We therefore explored a series of spacers featuring distinct functional groups of benzylammonium moieties (Fig. 2a), namely phenylmethylammonium iodide (PMAI), 2,3,4,5,6-(pentafluorophenyl) methylammonium iodide (*penta*-FPMAI) and (perfluoro-1,4-phenylene) dimethanammonium iodide (*tetra*-$FPDMAI_2$).

We examined 2D perovskite formation in the presence of such spacer cations, dynamically casting isopropanol solutions of organic halide salts onto $CsPbI_3$ perovskite films. The challenge in forming 2D perovskites on $CsPbI_3$ arises from the low solubility of CsI in isopropanol and the strong ionic bonding between Cs^+ and the $[PbI_6]^{4-}$ octahedral framework[17,34] (Supplementary Fig. 1). As shown in Fig. 2a, the photoluminescence (PL) spectra indicate that no distinct 2D perovskite emission is observed on the $CsPbI_3$ surface following post-treatment with PMAI. We infer that PMAI primarily remains adsorbed on the perovskite surface in its molecular form rather than forming a 2D perovskite structure (Supplementary Fig. 2). In contrast, the emerging PL peaks at about 488 nm for the films treated with *penta*-FPMAI and *tetra*-$FPDMAI_2$ reveal cation exchange with Cs^+ ions and the formation of 2D perovskites. Shoulders at lower energy (509 nm) may be assigned to the edge state commonly observed in 2D perovskites[35].

The formation of 2D/3D heterostructures is further corroborated by characteristic 2D perovskite diffraction peaks observed in the X-ray diffraction (XRD) patterns (Supplementary Fig. 3 and Supplementary Table 1). Incident-angle-dependent grazing-incidence wide-angle X-ray scattering (GIWAXS) images (Supplementary Figs. 4 and 5) show that the Bragg scattering rings at $q \approx 0.498$ $Å^{-1}$ for the $CsPbI_3$/(*tetra*-FPDMA)PbI_4 sample gradually disappear as the incident angle increases, indicating that the (*tetra*-FPDMA)PbI_4 layer is present only on the surface of $CsPbI_3$. Scanning electron microscope (SEM) images, PL maps and time-of-flight secondary ion mass spectrometry (ToF-SIMS) depth profile suggest the formation of a conformal 2D (*tetra*-FPDMA)PbI_4 layer on top of $CsPbI_3$ films, with an estimated thickness of ~ 3 nm (Supplementary Figs. 6–8).

https://doi.org/10.1038/s41560-025-01817-6

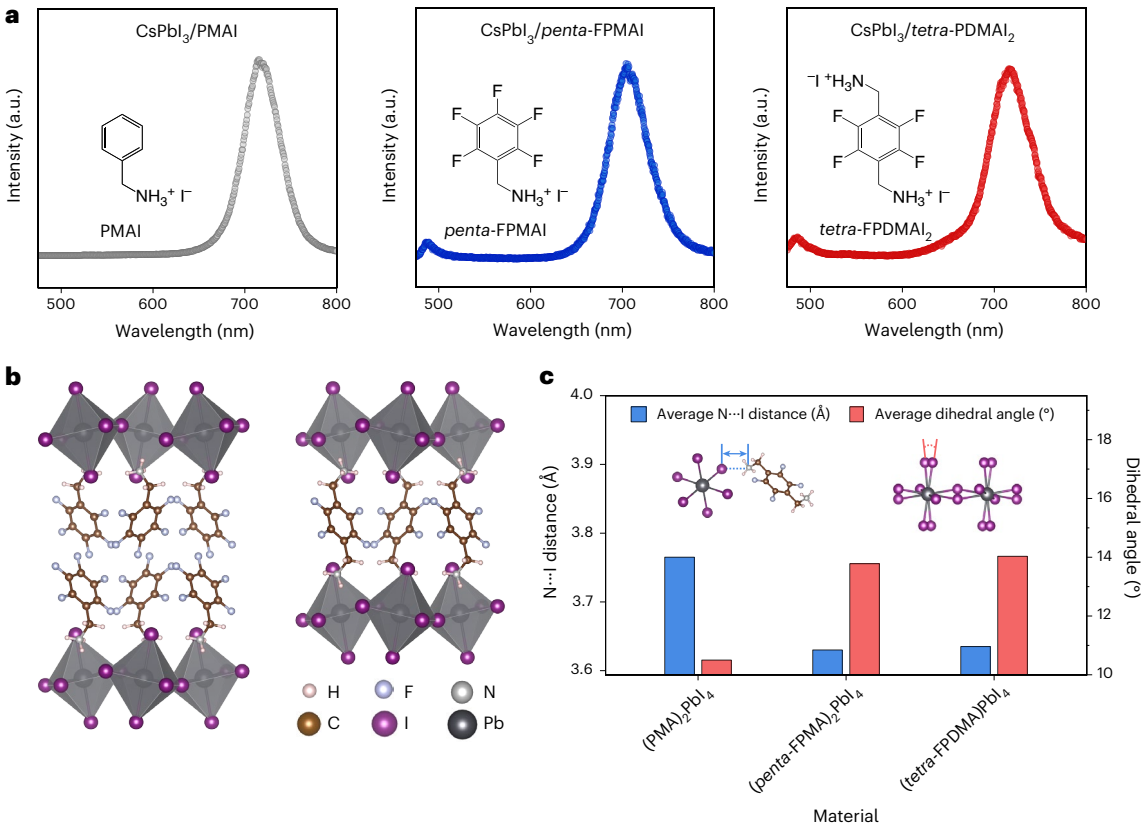

Fig. 2 | Perovskite heterostructures and single-crystal structural X-ray diffraction structures of the 2D perovskites. a, PL spectra of $CsPbI_3$ films post-treated with PMAI, *penta*-FPMAI and *tetra*-FPDMAI$_2$. **b**, Single-crystal X-ray diffraction structures of (*penta*-FPMA)$_2$PbI$_4$ (left) and (*tetra*-FPDMA)PbI$_4$ (right). **c**, Graph showing the average N···I distance and average dihedral angle in (PMA)$_2$PbI$_4$, (*penta*-FPMA)$_2$PbI$_4$ and (*tetra*-FPDMA)PbI$_4$.

To elucidate the formation of 2D/3D heterostructures, we analysed the structures of these 2D perovskites. Single crystals of (*penta*-FPMA)$_2$PbI$_4$ and (*tetra*-FPDMA)PbI$_4$ were synthesized and characterized by single-crystal X-ray diffraction after growth from slowly cooled saturated solutions of organic halide salts, PbO, HI and H_3PO_2 (Fig. 2b, Supplementary Fig. 9 and Supplementary Tables 2–17). We examined hydrogen bonding interactions between ammonium groups and $[PbI_6]^{4-}$ octahedra within 2D perovskites (Fig. 2c and Supplementary Table 2), finding average N···I distances of 3.77 Å, 3.63 Å and 3.64 Å for (PMA)$_2$PbI$_4$, (*penta*-FPMA)$_2$PbI$_4$ and (*tetra*-FPDMA)PbI$_4$, respectively[36,37]. This indicates that fluorination of the spacer cation, or the introduction of more electron withdrawing on the aromatic system, results in shorter (that is, stronger) hydrogen bonding interactions between -NH_3^+ and $[PbI_6]^{4-}$ as a result of the ammonium site holding more positive charge[38–40] (Supplementary Fig. 10). This improved hydrogen bonding of ammonium groups enhances the ability of cations to replace Cs^+ and occupies $[PbI_6]^{4-}$ octahedral frames during the post-treatment process, facilitating the formation of 2D layers on $CsPbI_3$ surfaces.

We analysed the crystal structures of the 2D perovskites and summarized their dihedral angles and average lattice misfit levels (f_{ave}) relative to $CsPbI_3$ (refs. 41,42; Supplementary Table 18). In both (*penta*-FPMA)$_2$PbI$_4$ and (*tetra*-FPDMA)PbI$_4$, the lead iodide layers are distorted appreciably, exhibiting a $[PbI_6]^{4-}$ dihedral angle (that is, out-of-plane tilting) of 13.7 and 14.0°, respectively, substantially greater than 10.5° observed in (PMA)$_2$PbI$_4$ (refs. 34,43). The dihedral angle of (*penta*-FPMA)$_2$PbI$_4$ and (*tetra*-FPDMA)PbI$_4$ closely approaches that of $CsPbI_3$ (14.95°). Additionally, (*tetra*-FPDMA)PbI$_4$ exhibits the lowest f_{ave} of 1.65% among these 2D perovskites, with (*penta*-FPMA)$_2$PbI$_4$ and (PMA)$_2$PbI$_4$ showing f_{ave} values of 1.85% and 2.35%, respectively. This suggests a quasi-epitaxial relationship between $CsPbI_3$ and the highly fluorinated 2D perovskites, which further facilitates the construction of 2D/3D heterostructures[41,42,44]. Further investigation of surface passivation via the thermal evaporation method confirmed that solvent effects on heterostructure formation are negligible (Supplementary Fig. 11). Instead, the enhanced hydrogen bonding, coupled with quasi-epitaxial alignment, serves as the primary driving force governing heterostructure formation in inorganic perovskite systems.

Exploring stable 2D perovskite materials

While fluorination of the spacer cation facilitates the formation of 2D layers on $CsPbI_3$ surfaces, it remains uncertain whether these cations will migrate into the 3D perovskite bulk, particularly under heating—a phenomenon commonly observed with other widely used spacer cations[26–29].

We evaluated the intrinsic stability of 2D perovskites by calculating cation desorption energies using density functional theory (Fig. 3a). The 2D perovskites with additional anchoring groups (*tetra*-FPDMA)PbI$_4$ exhibit cation desorption energies of 18.1 eV. This value is nearly double those of 2D perovskites with a single anchoring group, such as (*penta*-FPMA)$_2$PbI$_4$ and (PMA)$_2$PbI$_4$, which have desorption energies of 10.0 eV and 9.1 eV, respectively. Furthermore, (*penta*-FPMA)$_2$PbI$_4$ exhibits higher cation desorption energies than its non-fluorinated 2D perovskite (PMA)$_2$PbI$_4$, suggesting the incorporation of fluorine into the spacer cation may further enhance the structure stability of 2D perovskites.

We established an accelerated experiment to investigate the stability of 2D perovskites in environments enriched with Cs, as depicted in Fig. 3b. The 2D perovskite films of (PMA)$_2$PbI$_4$, (*penta*-FPMA)$_2$PbI$_4$ and (*tetra*-FPDMA)PbI$_4$ were fabricated by spin coating

https://doi.org/10.1038/s41560-025-01817-6

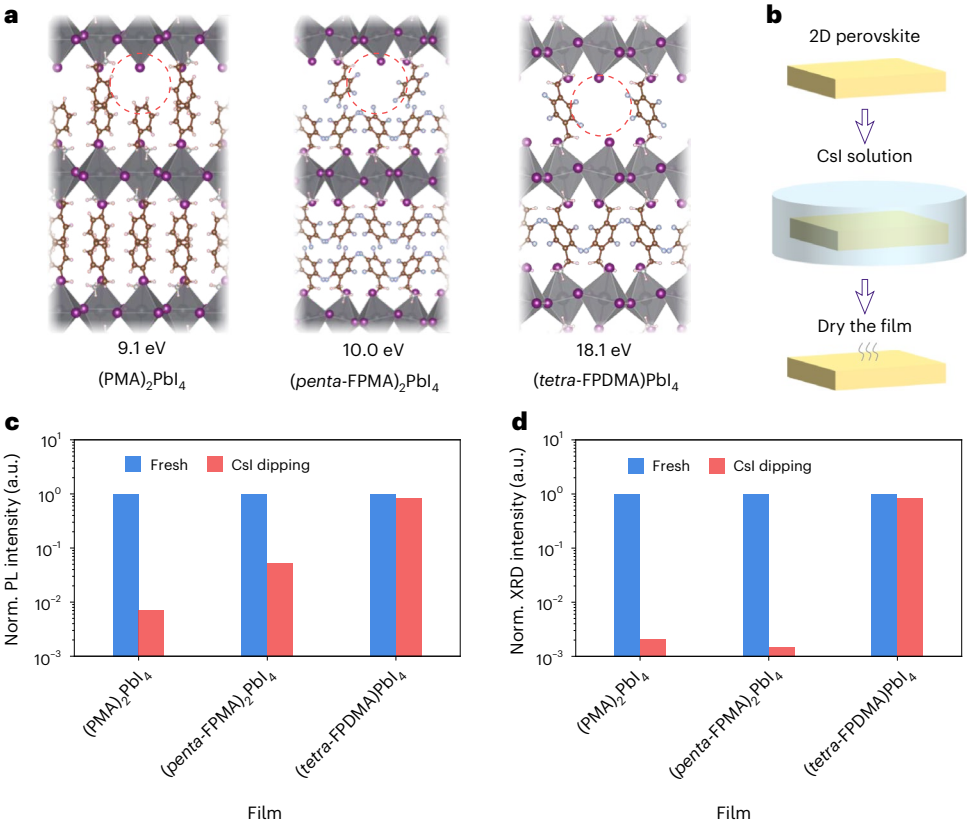

Fig. 3 | Stability of 2D perovskite materials under Cs-rich environments. **a**, Cation desorption energies of the $(PMA)_2PbI_4$, (*penta*-FPMA)$_2PbI_4$ and (*tetra*-FPDMA)PbI_4 2D perovskites. The red dashed circles indicate cation vacancies. **b**, Schematic illustrating the investigation of ion diffusion in 2D perovskite films, where the films are immersed in the CsI/isopropanol solution. **c**,**d**, Normalized characteristic PL peak intensity at 530 nm, 487 nm and 489 nm (**c**) and normalized characteristic XRD peak intensity at 6.1°, 5.0° and 6.8° for the $(PMA)_2PbI_4$, (*penta*-FPMA)$_2PbI_4$ and (*tetra*-FPDMA)PbI_4 films, respectively, before and after dipping in a CsI/isopropanol solution (**d**). 'Norm.' denotes normalization to the intensity of the fresh sample. Further information is available in Supplementary Figs. 12 and 13.

N,*N*-dimethylformamide (DMF) solutions containing the respective benzylammonium iodide salts and PbI_2 onto glass substrates.

PL spectra (Fig. 3c and Supplementary Fig. 12) reveal that upon immersion in a saturated CsI/isopropanol solution for 60 s, both $(PMA)_2PbI_4$ and (*penta*-FPMA)$_2PbI_4$ films lost their characteristic emission peaks at 530 nm and 487 nm, respectively. XRD patterns (Fig. 3d and Supplementary Fig. 13) confirmed the complete disappearance of their 2D perovskite phase, with yellow (δ) phase $CsPbI_3$ and PbI_2 diffraction peaks observed. Conversely, the (*tetra*-FPDMA)PbI_4 film retained about 85% of its initial PL emission at 489 nm. Substituting CsI with formamidinium iodide (FAI) yielded similar results (Supplementary Fig. 14). These results suggest that ligands with more anchoring groups can enhance the structural stability of 2D perovskites in a Cs/FA-rich environment.

We utilized 1,4-phenylenediammonium iodide ($PDMAI_2$) to further test the aforementioned findings. Post-treatment with $PDMAI_2$ does not facilitate the formation of 2D perovskite on the $CsPbI_3$ surface (Supplementary Fig. 15), resulting from the weaker bonding between $-NH_3^+$ and $[PbI_6]^{4-}$, as evidenced by the longer average N···I distance of 3.75 Å in $(PDMA)PbI_4$, compared to 3.64 Å in the fluorinated 2D perovskite (*tetra*-FPDMA)PbI_4[36]. Additionally, the standalone $(PDMA)PbI_4$ film retained 76% of its initial PL at 525 nm after dipping in CsI, despite quasi-2D phase emissions (Supplementary Fig. 16), due to its higher cation desorption energy of 16.5 eV, surpassing that of the mono-ammonium-based $(PMA)_2PbI_4$ (Supplementary Fig. 17).

Stability of the 2D/3D heterostructures

To assess the stability of the 2D/3D heterostructures, we performed the X-ray photoelectron spectroscopy (XPS) depth profile analysis on the both fresh and aged samples of $CsPbI_3$/(*penta*-FPMA)$_2PbI_4$ and $CsPbI_3$/(*tetra*-FPDMA)PbI_4 (Fig. 4a). After post-annealing at 85 °C for 5 h, the F 1*s* XPS peak dramatically decreased in the $CsPbI_3$/(*penta*-FPMA)$_2PbI_4$ sample, whereas the $CsPbI_3$/(*tetra*-FPDMA)PbI_4 sample maintained its peak intensity well under the same ageing conditions. We also conducted ToF-SIMS on these samples (Fig. 4b). We found that after ageing, the signal of *penta*-$FPMA^+$ decreased at the film surface while increasing in the bulk, suggesting migration of the spacer cation in the $CsPbI_3$/(*penta*-FPMA)$_2PbI_4$ sample. Conversely, the distribution of the spacer associated with *tetra*-$FPDMA^{2+}$ remained relatively stable, indicating enhanced stability of the $CsPbI_3$/(*tetra*-FPDMA)PbI_4 heterostructure.

Time-dependent PL spectra of the $CsPbI_3$/(*penta*-FPMA)$_2PbI_4$ sample showed an initial emission at 487 nm attributed to (*penta*-FPMA)$_2PbI_4$ with a monolayer thickness ($n = 1$), which faded over time. Concurrently, emissions above 575 nm corresponding to 2D phases with higher n values gradually increased (Fig. 4c). These results indicate that the (*penta*-FPMA)$_2PbI_4$ 2D perovskite structure is thermodynamically unstable in a Cs^+-rich environment, leading to Cs^+ incorporation and transformation of the 2D structure over time, that is, cation migration between 2D and 3D layers. Notably, this cation migration was observed to occur faster than the phase degradation of black-phase $CsPbI_3$ under damp heat conditions (Supplementary Fig. 18). In contrast, the $CsPbI_3$/(*tetra*-FPDMA)PbI_4 sample, featuring two anchoring groups and four fluorine groups, exhibited a stable PL emission at 489 nm over time.

Device performance and stability

We assessed the energy level alignments of the perovskite heterostructures using ultraviolet photoelectron spectroscopy and ultraviolet–visible spectra (Fig. 5a and Supplementary Figs. 19 and 20).

https://doi.org/10.1038/s41560-025-01817-6

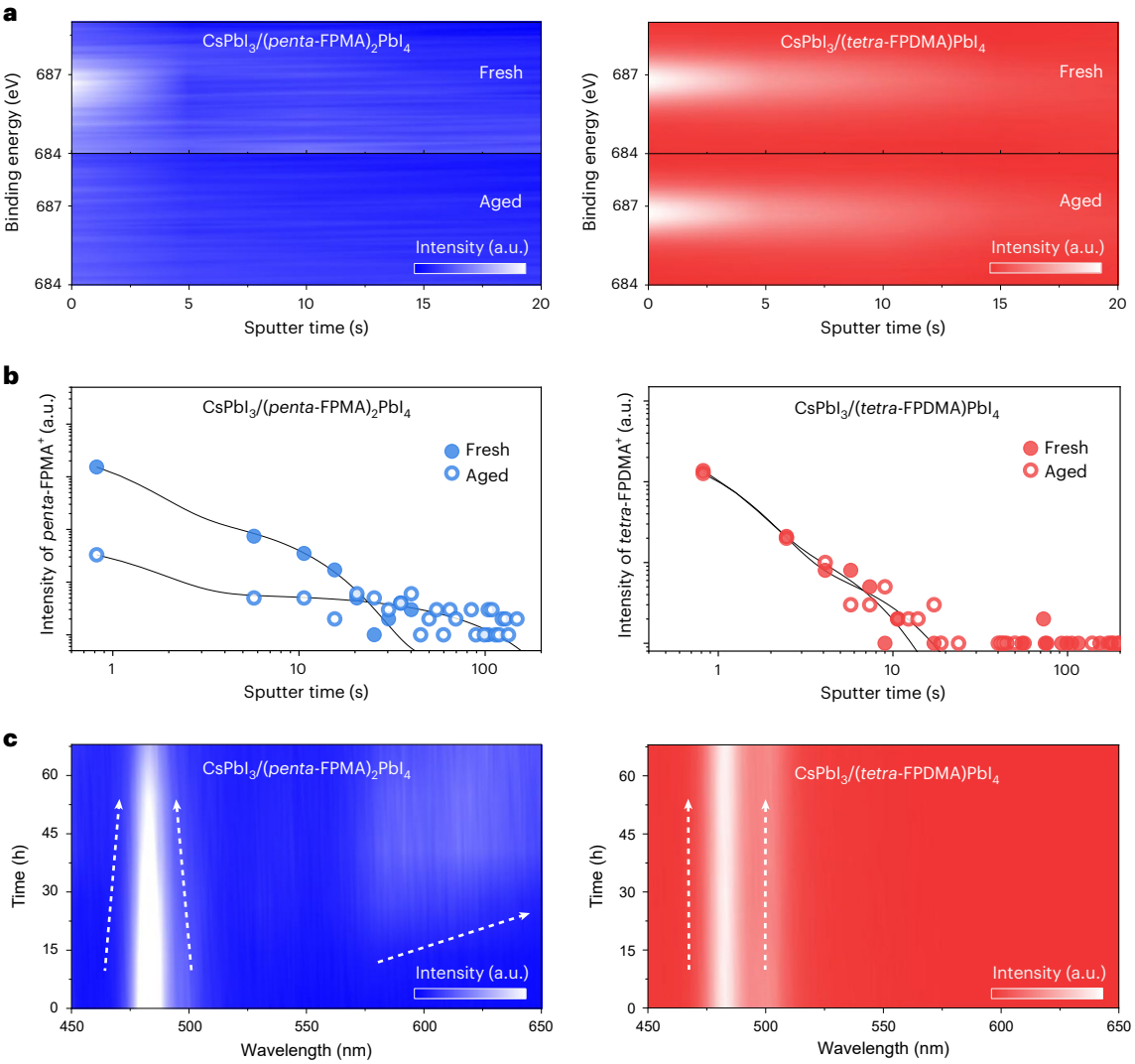

Fig. 4 | Stability of the 2D/3D heterostructures. a, F 1*s* XPS depth profiles of $CsPbI_3$/(*penta*-FPMA)$_2PbI_4$ and $CsPbI_3$/(*tetra*-FPDMA)PbI_4 films before and after ageing at 85 °C for 5 h. Colour scale indicates XPS intensity (a.u.): 260,000–280,000 (*penta*-FPMA, fresh), 240,000–280,000 (*penta*-FPMA, aged), 220,000–390,000 (*tetra*-FPDMA, fresh) and 210,000–370,000 (*tetra*-FPDMA, aged). **b**, ToF-SIMS of $CsPbI_3$/(*penta*-FPMA)$_2PbI_4$ and $CsPbI_3$/(*tetra*-FPDMA)PbI_4 films before and after ageing at 85 °C for 5 h. **c**, Time-dependent PL images of $CsPbI_3$/(*penta*-FPMA)$_2PbI_4$ and $CsPbI_3$/(*tetra*-FPDMA)PbI_4 films. Colour scale indicates PL intensity (a.u.): 0–12,000 for *penta*-FPMA and 0–40,000 for *tetra*-FPDMA.

The (*tetra*-FPDMA)PbI_4 layer exhibits a higher conduction band and a marginally higher valence band compared to the $CsPbI_3$ perovskite, which is advantageous as it blocks electrons while facilitating hole transport. On the other hand, (*penta*-FPMA)$_2PbI_4$ presents a slight energy mismatch (0.12 eV) in the valence band at the interface.

We also analysed film uniformity by examining the PL intensity distribution on $CsPbI_3$ films (Fig. 5b and Supplementary Fig. 21). The narrower PL intensity distribution observed in the $CsPbI_3$/(*tetra*-FPDMA)PbI_4 sample indicates greater spatial homogeneity compared to both $CsPbI_3$/(*penta*-FPMA)$_2PbI_4$ and $CsPbI_3$ samples.

The photovoltaic performance of the $CsPbI_3$ PSCs was investigated in a regular n–i–p configuration comprising fluorine-doped tin oxide (FTO)/TiO_x/SnO_x/$CsPbI_3$/(*tetra*-FPDMA)PbI_4/2,2′,7,7′-tetrakis[*N*,*N*-di(4-methoxyphenyl)amino]-9,9′-spirobifluorene (spiro-OMeTAD)/Au as shown in the cross-section SEM image (Supplementary Fig. 22). The best-performing device, based on (*tetra*-FPDMA)PbI_4, exhibits a PCE of 21.6%, compared to 20.2% and 20.9% for the control and (*penta*-FPMA)$_2PbI_4$-passivated $CsPbI_3$ PSCs (Fig. 5c,d and Supplementary Fig. 23), respectively, with a steady-state efficiency of 21.1% (Supplementary Fig. 24).

To investigate the passivation effects of (*tetra*-FPDMA)PbI_4 perovskite in large-area devices, $CsPbI_3$ perovskite modules consisting of eight interconnected sub-cells in a series configuration were constructed (Supplementary Fig. 25). With the 2D/3D heterojunction, the best-performing module achieved a PCE of 19.8% (corresponding to an aperture-area PCE of 18.4%) over an active area of 16.0 cm^2 and a low cell-to-module PCE loss of 2% (absolute), exhibiting negligible hysteresis (Fig. 5e). The module was evaluated by the Photovoltaic Laboratory of the Institute of Micro Technique (IMT), Neuchâtel, Switzerland, and an active-area PCE of 18.8% (corresponding to an aperture-area PCE of 17.5%) was obtained (Supplementary Fig. 26). The external quantum efficiency spectrum (Supplementary Fig. 27) demonstrated a bandgap of ~1.7 eV. As the size was increased to an active area of 28.2 cm^2, a high PCE of 18.7% was obtained (Supplementary Fig. 28). To the best of our knowledge, these modules have the highest reported PCEs among inorganic-based perovskite modules[2,20,45–52] (Fig. 5f).

To evaluate the device stability, we measured the ToF-SIMS of the device after ageing at 85 °C for 24 h (Fig. 5g and Supplementary Fig. 29). We found that Li ions from the spiro-OMeTAD layer tend to

https://doi.org/10.1038/s41560-025-01817-6

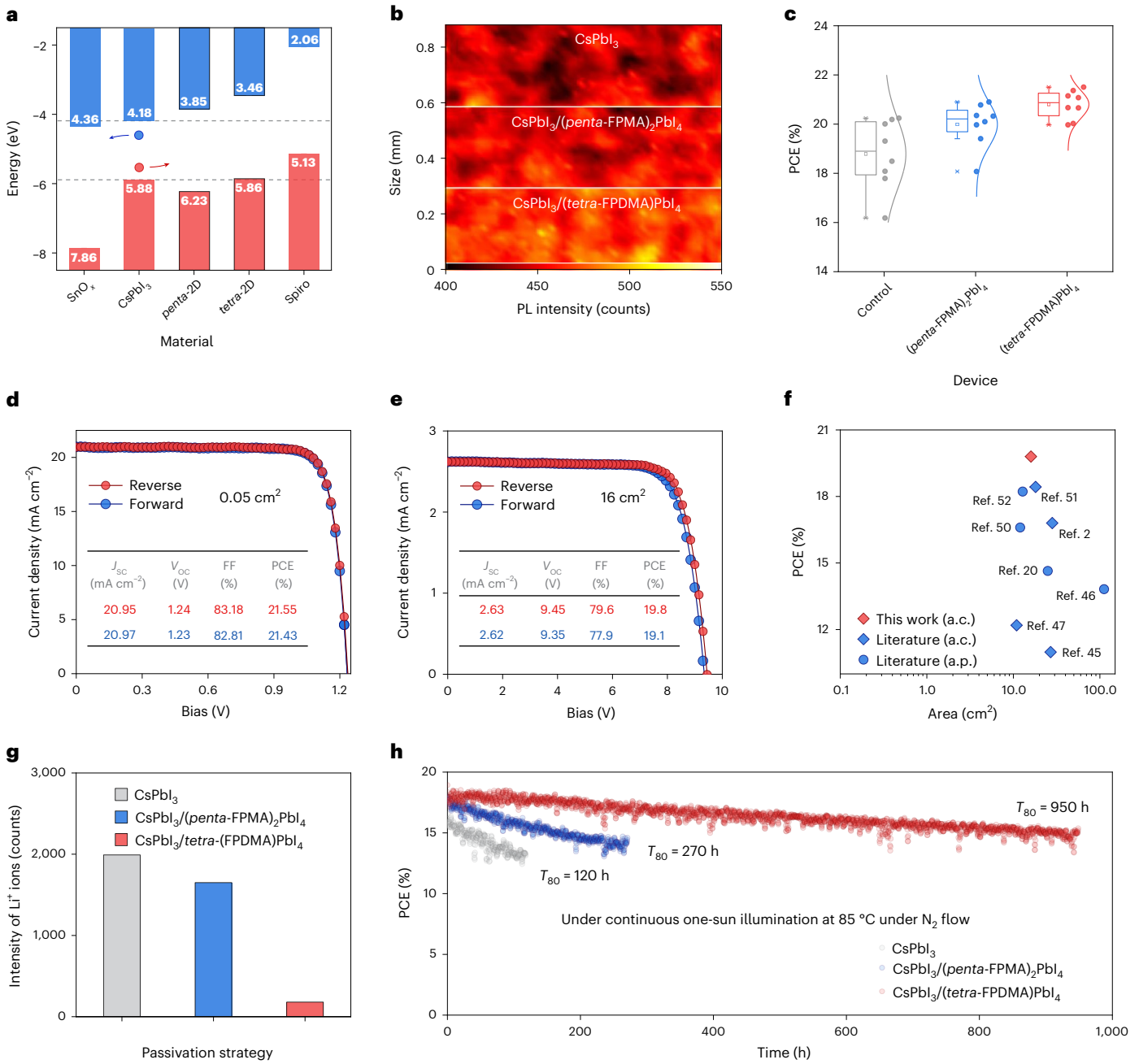

Fig. 5 | Photovoltaic performance and stability. a, Energy level diagram of the perovskite heterojunctions with charge transport materials. Blue and red dots represent electrons and holes, respectively, and the arrows indicate their transport directions. **b**, PL mapping images of the control-, (*penta*-FPMA)$_2$PbI$_4$- and (*tetra*-FPDMA)PbI$_4$-based CsPbI$_3$ films. Colour scale indicates PL intensity from 400 to 550 counts. **c**, Efficiency statistics of PSCs as a function of passivation strategy, evaluated across 8 devices for each condition ($n = 8$; biological replicates). In the boxplots, the mean (open square), median (centre line), 1st and 99th percentiles (×) and whiskers (outliers) are shown. **d**,**e**, *J*–*V* characteristics of the best-performing (*tetra*-FPDMA)PbI$_4$-based CsPbI$_3$ PSC (**d**) and module (**e**) with active areas of 0.05 cm^2 and 16.0 cm^2, respectively. J_{SC} is the short-circuit current density and V_{OC} is the open-circuit voltage. FF, fill factor. **f**, Summary of the PCEs for the state-of-the-art inorganic-perovskite-based solar modules[2,20,45–52] (Supplementary Table 19). a.c., active area; a.p., aperture area. **g**, Intensity of Li$^+$ ion migration into perovskite films with different passivation strategies after ageing at 85 °C for 24 h. **h**, MPP tracking for devices operating at 85 °C under illumination with simulated AM 1.5 G illumination (100 mW cm^{-2}) using a light-emitting diode light source in N_2. The initial efficiencies of the control-, (*penta*-FPMA)$_2$PbI$_4$- and (*tetra*-FPDMA)PbI$_4$-based devices were 16.6%, 18.0% and 18.9%, respectively. T_{80} denotes the time required for the device to reach 80% of its initial PCE.

migrate into perovskite films during ageing, especially in the control and (*penta*-FPMA)$_2$PbI$_4$ devices. The (*tetra*-FPDMA)PbI$_4$-based device, however, showed less Li ion migration, indicating the blocking effect of the (*tetra*-FPDMA)PbI$_4$ layer at the perovskite/HTL interface. Additionally, the (*tetra*-FPDMA)PbI$_4$ capping layer plays a key role in reducing the moisture penetration and suppressing phase degradation (Supplementary Fig. 30). Humidity stability tests were performed on devices without encapsulation under ambient conditions with a relative humidity of ~50%. The *tetra*-FPDMAPbI$_4$ capping layers enhanced device stability, achieving a PCE retention of 83% after 300 h of ageing, compared to 64% and 54% for (*penta*-FPMA)$_2$PbI$_4$ and control devices, respectively (Supplementary Fig. 31).

We then investigated the long-term operating stability of encapsulated devices by maximum power point tracking under continuous AM 1.5 G illumination at 85 °C in a N_2 environment. Unstable spiro-OMeTAD was replaced with poly[bis(4-phenyl)(2,4,6-trimethylphenyl)amine] to eliminate the hole transport layer as a source of instability[16]. The (*tetra*-FPDMA)PbI_4-based device shows a T_{80} lifetime (representing the time it takes to reach 80% of the initial PCE) of 950 h (Fig. 5h), considerably surpassing the (*penta*-FPMA)$_2PbI_4$-based and control devices, which exhibited 270 h and 120 h, respectively. The (*tetra*-FPDMA)PbI_4-based module also demonstrated superior stability under light illumination at 65 °C, retaining 80% of initial efficiency after 500 h (Supplementary Fig. 32). This stability enhancement comes from the dual role of the 2D capping layer: the layer extends the lifetime of surface passivation by preventing the degradation of the 3D/2D heterojunction; and it improves the phase stability of the underlying 3D perovskite, suppressing surface lattice distortion and preventing water-induced phase degradation.

Conclusions

We demonstrated the mechanisms behind the formation and stabilization of 2D/3D heterostructures on inorganic perovskite surfaces: the formation of heterostructures is primarily driven by the interactions between ammonium groups and $[PbI_6]^{4-}$ octahedra, whereas their stabilization hinges on the interactions between entire spacer cations and $[PbI_6]^{4-}$ octahedra. We incorporated electron-withdrawing fluorine to increase the positive charge at the ammonium site, promoting cation exchange with Cs for the heterostructure formation, while introducing extra anchoring groups to strengthen the interaction between spacer cations and $[PbI_6]^{4-}$ octahedra, thereby immobilizing the cations and stabilizing the heterostructures at elevated temperatures. This approach enhances the efficiency of inorganic PSCs and modules while ensuring their stable operation at elevated temperatures. These results underscore the transformative potential of rational cation design in producing stable 2D/3D heterostructures that enhance both the performance and stability of perovskite optoelectronics.

Methods

Materials and methods

Lead iodide (PbI_2, 99.99%) was purchased from Tokyo Chemical Industry. Caesium iodide (CsI, >99.9%) and 2,2′,7,7′-tetrakis(*N*,*N*-di-*p*-methoxyphenyl-amino)-9,9′-spirobifluorene (spiro-OMeTAD, 99.9%) were purchased from the Xi'an Polymer Light Technology Corp. Hydroiodic acid (57 wt% in water), chlorobenzene (99.8%), *N*,*N*-dimethylformamide (DMF, 99.9%), dimethyl sulfoxide (DMSO, 99.9%), titanium diisopropoxide bis(acetylacetonate) (TAA, 75 wt% in isopropanol), diethyl ether (99%), 4-*tert*-butylpyridine (TBP, 98%), acetonitrile (99.8%) and isopropanol (99.5%) were purchased from Sigma-Aldrich. $SnCl_4$ (99%) was ordered from Acros Organics. Lithium bis(trifluoromethane)sulfonamide (LiTFSI), FK 209 Co(III) TFSI and $PDAI_2$ were purchased from Greatcell Solar Materials. All reagents were used as received without further purification. $DMAPbI_3$ was prepared by reaction of PbI_2 and hydroiodic acid in DMF[45]. PMAI[53] and *penta*-FPMAI[54] were prepared as previously reported. Synthesis procedures of *tetra*-$FPDMAI_2$ were described in Supplementary Fig. 33.

Synthesis of single crystals

Single crystals of (*tetra*-FPDMA)PbI_4 and (*penta*-FPMA)$_2PbI_4$ were synthesized by combining 0.1 mmol (23.3 mg) PbO and 0.1 mmol (45.9 mg) (*tetra*-FPDMA)I_2 or 0.2 mmol (65.0 mg) (*penta*-FPMA)I in a vial with approximately 4 ml HI (57% w/w) and 0.25 ml H_3PO_2 (50% w/w). The solution was heated to 200 °C on a hot plate with stirring until all solid was dissolved. Once dissolved, the temperature was lowered to 130 °C for 1 day, and then the hot plate was turned off and the solution left to cool to room temperature. After equilibrating at room temperature, crystals were picked directly from the acid solution and suspended in paratone oil for the single-crystal XRD measurements.

X-ray crystallography

Intensity data of a plate single crystals of (*tetra*-FPDMA)PbI_4 was collected at 300 K. A suitable single crystal with dimensions of approximately 0.5 × 0.5 × 0.5 mm^3 was mounted on a glass fibre with paratone oil on a STOE StadiVari diffractometer equipped with an AXO Ag Kα micro-focus sealed X-ray A-MiXS source (λ = 0.560834 Å), running at 65 kV and 0.68 mA, and a Dectris Pilatus3 R CdTe 300 K Hybrid Photon Counting detector. Data reduction was performed with the X-Area software package using numerical absorption correction using X-Shape. The structures were solved with the ShelXT structure solution programme using the Intrinsic Phasing solution method and by using Olex2 as the graphical interface. The models were refined with ShelXL using least-squares minimization.

Intensity data of plate single crystals of (*penta*-FPMA)$_2PbI_4$ was collected at 293 K using a STOE imaging plate diffraction system (IPDS-II) with graphite-monochromated Mo Kα radiation operating at 50 kV and 40 mA with a 34 cm image plate. The X-AREA, X-RED and X-SHAPE software packages were used for data extraction and integration and to apply analytical absorption corrections. Direct methods and full-matrix least-squares refinement against F2 were performed with the SHELXTL package.

Device fabrication. FTO substrates were cleaned using detergent, deionized water, acetone and isopropanol by an ultrasonic cleaner. The TiO_x layer was obtained by spray pyrolysis in ambient air using a diluted solution of TAA in isopropanol (1:15, volume ratio) at 450 °C, followed by annealing for 30 min. After cooling down, 0.1 M $SnCl_4$ aqueous solution was deposited on the substrate at 3,000 rpm for 30 s and the SnO_x films were dried at 190 °C for 1 h. Then the substrates were transferred into the nitrogen glovebox for film deposition. The 0.7 M $CsPbI_3$ precursor solution was prepared by dissolving CsI and $DMAPbI_3$ with a 1:1 molar ratio in DMF and DMSO mixed solvent with a 9:1 volume ratio. $CsPbI_3$ films were prepared by spin coating 30 µl precursor solution at 1,000 rpm for 10 s with a ramping rate of 200 rpm s^{-1} and at 2,500 rpm for 30 s with a ramping rate of 1,000 rpm s^{-1}. The substrates were taken out from the glovebox and put onto a hotplate in ambient at 180 °C for 25 min to obtain uniform $CsPbI_3$ films. For post treatment, 10 mM organic halide salts were dissolved in isopropanol and the 100 µl solution was dynamically spin coated at 5,000 rpm for 20 s, followed by annealing at 100 °C for 2 min. Dynamically spin coating involves the process of introducing the solution while the substrate is in spinning. The spiro-OMeTAD solution was prepared by dissolving 75 mg spiro-OMeTAD in chlorobenzene with 32 µl TBP, 20 µl LiTFSI in acetonitrile (1.8 M) and 8 µl FK209 in acetonitrile (1 M). Then 35 µl spiro-OMeTAD solution was spin coated on the perovskite substrates at 3,000 rpm for 20 s. Finally, 70 nm Au was thermally evaporated as the electrode.

Module fabrication. The fabrication process for each layer is the same as that of the small-area PSCs except for the amount of precursors for spin coating. The 200 µl perovskite solution, 300 µl post-treatment solution and 300 µl spiro-OMeTAD solution were used for module fabrication. FTO substrates were patterned by a 1,064 nm Yb fibre laser (Trotec) with nine sub-cells connected in series. The laser power for P1, P2 and P3 were 12 W, 3 W and 3 W, respectively.

Density functional theory calculation. All density functional theory (DFT) calculations were performed using the Vienna Ab initio Software Package version 6.2.1[55]. The Perdew–Burke–Ernzerhof functional was used for all calculations and augmented with Grimme's D3 empirical correction for London Dispersion forces[56,57]. Projector augmented wave pseudopotentials were used to describe all atoms[58]. 1 × 3 × 3 K point

grids in Monkhorst-Pack schemes were used for all calculations. Experimentally determined crystal structures were used as starting points for all geometry optimizations, in which atom positions, cell volumes and cell shapes were all degrees of freedom. For defect states, the cell shape and cell volume were kept identical to the analogous pristine crystal lattices. A wavefunction energy cut-off of 1×10^{-6} eV was adopted along with a force cut-off of 0.02 eV $Å^{-1}$.

Characterization. ^{1}H NMR spectra were recorded at 400 MHz on a Bruker Avance III spectrometer with a 5 mm double resonance broad band BBO z-gradient room temperature probe, ^{13}C NMR spectra were collected using the same instrument at 101 MHz. The chemical shifts, expressed in ppm, were relative to tetramethylsilane. All nuclear magnetic resonance (NMR) experiments were performed at 25 °C. Reactions were monitored by thin-layer chromatography on ALUGRAM SIL G/UV254 plates and developed with UV light. Silica gel (grade 9385, 230–400 mesh, 60 Å, Aldrich) was used for column chromatography. Elemental analysis was performed with an Exeter Analytical CE-440 elemental analyser, Model 440 C/H/N/. MS were recorded on Waters SQ Detector 2 Spectrometer using the electrospray ionization technique. The PL spectra were collected using a confocal Raman system (excitation wavelength = 473 nm) integrated with SWIFT and DuoScan technologies. GIWAXS was recorded through a Huber diffractometer and photon energy of 12.39 keV (1.0 Å) at beamline BL19B2 of SPring-8 with PILATUS 300 K 2D X-ray detectors. FEI Sirion-200 scanning electron microscope was used to get scanning electron microscopy images. Ultraviolet photoelectron spectroscopy was performed on the perovskite films on glass substrates using an AXIS Nova spectrometer (Kratos Analytical) with a He-I source (21.22 eV). ToF-SIMS was performed using an IONTOF M6 instrument with a Bi_3^+ (30 keV) primary ion beam. Current density (*J*)–voltage (*V*) characteristics were measured with a solar simulator (Oriel, 450 W xenon, AAA class) and a Keithley 2400 source meter. A Si reference cell (KG5, Newport) was used for calibration before measurements to ensure the AM 1.5 G standard. For small-area PSCs, the voltage scan rate and scan steps were 100 mV s^{-1} and 20 mV, respectively, and the active area was 0.049 cm^2. For perovskite solar modules, the voltage scan rate was 200 mV s^{-1} and scan step was 50 mV, and the aperture areas were 17.20 cm^2 and 30.74 cm^2, respectively. External quantum efficiency spectra were measured using IQE200B (Oriel). The maximum power point tracking measurement was conducted on encapsulated devices under light-emitting diode illumination (100 mW cm^{-2}) at 85 °C with N_2 flow.

Reporting summary

Further information on research design is available in the Nature Portfolio Reporting Summary linked to this article.

Data availability

The data that support the findings of this study are provided in Supplementary Information. Source data are provided with this paper.

References

1. Wang, Y. et al. Thermodynamically stabilized β-$CsPbI_3$-based perovskite solar cells with efficiencies >18%. *Science* **365**, 591–595 (2019).
2. Liu, C. et al. Retarding solid-state reactions enable efficient and stable all-inorganic perovskite solar cells and modules. *Sci. Adv.* **9**, eadg0087 (2023).
3. Swarnkar, A. et al. Quantum dot-induced phase stabilization of α-$CsPbI_3$ perovskite for high-efficiency photovoltaics. *Science* **354**, 92–95 (2016).
4. Gu, H. et al. Phase-pure two-dimensional layered perovskite thin films. *Nat. Rev. Mater.* **8**, 533–551 (2023).
5. Zhao, X. et al. Accelerated aging of all-inorganic, interface-stabilized perovskite solar cells. *Science* **377**, 307–310 (2022).
6. Chen, H. et al. Improved charge extraction in inverted perovskite solar cells with dual-site-binding ligands. *Science* **384**, 189–193 (2024).
7. Wang, Z. et al. Managing multiple halide-related defects for efficient and stable inorganic perovskite solar cells. *Angew. Chem. Int. Ed.* **62**, e202305815 (2023).
8. Sun, X. et al. Highly efficient $CsPbI_3/Cs_{1-x}DMA_xPbI_3$ bulk heterojunction perovskite solar cell. *Joule* **6**, 850–860 (2022).
9. Chu, X. et al. Surface in situ reconstruction of inorganic perovskite films enabling long carrier lifetimes and solar cells with 21% efficiency. *Nat. Energy* **8**, 372–380 (2023).
10. Tan, S. et al. Temperature-reliable low-dimensional perovskites passivated black-phase $CsPbI_3$ toward stable and efficient photovoltaics. *Angew. Chem. Int. Ed.* **61**, e202201300 (2022).
11. Li, T. et al. Inorganic wide-bandgap perovskite subcells with dipole bridge for all-perovskite tandems. *Nat. Energy* **8**, 610–620 (2023).
12. Mali, S. S. et al. All-inorganic halide perovskites for air-processed "n–i–p" monolithic perovskite/organic hybrid tandem solar cells exceeding 23% efficiency. *Energy Environ. Sci.* **17**, 1046–1060 (2024).
13. Wang, Z. et al. Suppressed phase segregation for triple-junction perovskite solar cells. *Nature* **618**, 74–79 (2023).
14. Wang, X., Wang, Y., Chen, Y., Liu, X. & Zhao, Y. Efficient and stable $CsPbI_3$ inorganic perovskite photovoltaics enabled by crystal secondary growth. *Adv. Mater.* **33**, 2103688 (2021).
15. Zhang, Z. et al. Rationalization of passivation strategies toward high-performance perovskite solar cells. *Chem. Soc. Rev.* **52**, 163–195 (2023).
16. Yang, Y. et al. A thermotropic liquid crystal enables efficient and stable perovskite solar modules. *Nat. Energy* **9**, 316–323 (2024).
17. Liu, C. et al. Bimolecularly passivated interface enables efficient and stable inverted perovskite solar cells. *Science* **382**, 810–815 (2023).
18. Steele, J. A. et al. Thermal unequilibrium of strained black $CsPbI_3$ thin films. *Science* **365**, 679–684 (2019).
19. Sutton, R. J. et al. Cubic or orthorhombic? Revealing the crystal structure of metastable black-phase $CsPbI_3$ by theory and experiment. *ACS Energy Lett.* **3**, 1787–1794 (2018).
20. Heo, J. H. et al. Surface engineering with oxidized $Ti_3C_2T_x$ MXene enables efficient and stable p–i–n-structured $CsPbI_3$ perovskite solar cells. *Joule* **6**, 1672–1688 (2022).
21. Wu, L. et al. Stabilization of inorganic perovskite solar cells with a 2D Dion–Jacobson passivating layer. *Adv. Mater.* **35**, 2304150 (2023).
22. Du, Y. et al. Manipulating the formation of 2D/3D heterostructure in stable high-performance printable $CsPbI_3$ perovskite solar cells. *Adv. Mater.* **35**, 2206451 (2023).
23. Liu, X. et al. Organic tetrabutylammonium cation intercalation to heal inorganic $CsPbI_3$ perovskite. *Angew. Chem. Int. Ed.* **60**, 12351–12355 (2021).
24. Wang, Y. et al. Efficient α-$CsPbI_3$ photovoltaics with surface terminated organic cations. *Joule* **2**, 2065–2075 (2018).
25. Sidhik, S. et al. Deterministic fabrication of 3D/2D perovskite bilayer stacks for durable and efficient solar cells. *Science* **377**, 1425–1430 (2022).
26. Sutanto, A. et al. In situ analysis reveals the role of 2D perovskite in preventing thermal-induced degradation in 2D/3D perovskite interfaces. *Nano Lett.* **20**, 3992–3998 (2020).
27. Szabó, G. & Kamat, P. V. How cation migration across a 2D/3D interface dictates perovskite solar cell efficiency. *ACS Energy Lett.* **9**, 193–200 (2024).

28. Perini, C. A. R. et al. Interface reconstruction from Ruddlesden–Popper structures impacts stability in lead halide perovskite solar cells. *Adv. Mater.* **34**, 2204726 (2022).
29. Liu, C. et al. Tuning structural isomers of phenylenediammonium to afford efficient and stable perovskite solar cells and modules. *Nat. Commun.* **12**, 6394 (2021).
30. Wang, Y., Zhang, T., Kan, M. & Zhao, Y. Bifunctional stabilization of all-inorganic α-$CsPbI_3$ perovskite for 17% efficiency photovoltaics. *J. Am. Chem. Soc.* **140**, 12345–12348 (2018).
31. Yoon, S. M. et al. Surface engineering of ambient-air-processed cesium lead triiodide layers for efficient solar cells. *Joule* **5**, 183–196 (2021).
32. Almalki, M. et al. Nanosegregation in arene-perfluoroarene π-systems for hybrid layered Dion–Jacobson perovskites. *Nanoscale* **14**, 6771–6776 (2022).
33. Li, X., Hoffman, J. M. & Kanatzidis, M. G. The 2D halide perovskite rulebook: how the spacer influences everything from the structure to optoelectronic device efficiency. *Chem. Rev.* **121**, 2230–2291 (2021).
34. Sun, H. et al. Surface defects management by in situ etching with methanol for efficient inverted inorganic perovskite solar cells. *Adv. Funct. Mater.* **33**, 2213913 (2023).
35. Sheikh, T., Shinde, A., Mahamuni, S. & Nag, A. Possible dual bandgap in $(C_4H_9NH_3)_2PbI_4$ 2D layered perovskite: single-crystal and exfoliated few-layer. *ACS Energy Lett.* **3**, 2940–2946 (2018).
36. Ummadisingu, A. et al. Multi-length scale structure of 2D/3D Dion–Jacobson hybrid perovskites based on an aromatic diammonium spacer. *Small* **18**, 2104287 (2022).
37. Papavassiliou, G. C., Mousdis, G. A., Raptopoulou, C. P. & Terzis, A. Preparation and characterization of $[C_6H_5CH_2NH_3]_2PbI_4$, $[C_6H_5CH_2CH_2SC(NH_2)_2]_3PbI_5$ and $[C_{10}H_7CH_2NH_3]PbI_3$ organic-inorganic hybrid compounds. *Z. Naturforsch. B.* **54**, 1405–1409 (1999).
38. Li, F. et al. Hydrogen-bond-bridged intermediate for perovskite solar cells with enhanced efficiency and stability. *Nat. Photonics* **17**, 478–484 (2023).
39. Lin, L. et al. Hydrogen bonding in perovskite solar cells. *Matter* **7**, 38–58 (2024).
40. Abate, A. et al. Supramolecular halogen bond passivation of organic–inorganic halide perovskite solar cells. *Nano Lett.* **14**, 3247–3254 (2014).
41. Han, C. et al. Impact and role of epitaxial growth in metal halide perovskite solar cells. *ACS Mater. Lett.* **5**, 2445–2463 (2023).
42. Hong, H. et al. Two-dimensional lead halide perovskite lateral homojunctions enabled by phase pinning. *Nat. Commun.* **15**, 3164 (2024).
43. Stoumpos, C. C. et al. Ruddlesden–Popper hybrid lead iodide perovskite 2D homologous semiconductors. *Chem. Mater.* **28**, 2852–2867 (2016).
44. Sidhik, S. et al. Two-dimensional perovskite templates for durable, efficient formamidinium perovskite solar cells. *Science* **384**, 1227–1235 (2024).
45. Liu, C. et al. Dopant-free hole transport materials afford efficient and stable inorganic perovskite solar cells and modules. *Angew. Chem. Int. Ed.* **60**, 20489–20497 (2021).
46. Heo, J. H. et al. Efficient and stable graded $CsPbI_{3-x}Br_x$ perovskite solar cells and submodules by orthogonal processable spray coating. *Joule* **5**, 481–494 (2021).
47. Liu, C. et al. Tailoring C_{60} for efficient inorganic $CsPbI_2Br$ perovskite solar cells and modules. *Adv. Mater.* **32**, 1907361 (2020).
48. Chen, R. et al. Moisture-tolerant and high-quality α-$CsPbI_3$ films for efficient and stable perovskite solar modules. *J. Mater. Chem. A* **8**, 9597–9606 (2020).
49. Heo, J. H. et al. Thermally stable inorganic $CsPbI_2Br$ mesoscopic metal halide perovskite solar submodules. *ACS Appl. Mater. Interfaces* **11**, 43066–43074 (2019).
50. Tan, S. et al. Constructing an interfacial gradient heterostructure enables efficient $CsPbI_3$ perovskite solar cells and printed minimodules. *Adv. Mater.* **35**, 2301879 (2023).
51. Mali, S. S. et al. Phase-heterojunction all-inorganic perovskite solar cells surpassing 21.5% efficiency. *Nat. Energy* **8**, 989–1001 (2023).
52. Liu, X. et al. $CsPbI_3$ perovskite solar module with certified aperture area efficiency >18% based on ambient-moisture-assisted surface hydrolysis. *Joule* **8**, 2851–2862 (2024).
53. Zhou, Q. et al. High-performance perovskite solar cells with enhanced environmental stability based on a $(p\text{-}FC_6H_4C_2H_4NH_3)_2[PbI_4]$ capping layer. *Adv. Energy Mater.* **9**, 1802595 (2019).
54. Paek, S. et al. Molecular design and operational stability: toward stable 3D/2D perovskite interlayers. *Adv. Sci.* **7**, 2001014 (2020).
55. Kresse, G. & Furthmüller, J. Efficient iterative schemes for ab initio total-energy calculations using a plane-wave basis set. *Phys. Rev. B* **54**, 11169–11186 (1996).
56. Perdew, J. P., Burke, K. & Ernzerhof, M. Generalized gradient approximation made simple. *Phys. Rev. Lett.* **77**, 3865–3868 (1996).
57. Grimme, S., Antony, J., Ehrlich, S. & Krieg, H. A consistent and accurate ab initio parametrization of density functional dispersion correction (DFT-D) for the 94 elements H–Pu. *J. Chem. Phys.* **132**, 154104 (2010).
58. Kresse, G. & Joubert, D. From ultrasoft pseudopotentials to the projector augmented-wave method. *Phys. Rev. B* **59**, 1758–1775 (1999).

Acknowledgements

M.K.N. acknowledges support from the European Union's Horizon 2020 research and innovation programme (number 763977). E.H.S. acknowledges support from the award 70NANB19H005 from the US Department of Commerce, National Institute of Standards and Technology, as part of the Center for Hierarchical Materials Design (CHiMaD). J.D.F. and M.G.K. acknowledge support from the National Science Foundation under grant number DMR-2019444 (National Science Foundation Center for Integration of Modern Optoelectronic Materials on Demand, IMOD, X-ray crystallographic and optical studies of 2D perovskites). I.W.G. was supported by US Department of Energy, Office of Science, Basic Energy Sciences, under award number DE-SC-0012541 (single-crystal X-ray crystal structure determination). K.R. thanks the Research Council of Lithuania via grant number S-MIP-20-20 and the funding received from the World Federation of Scientists (WFS) fellowship. This work made use of the EPIC facility of Northwestern University's NUANCE Center, which has received support from the SHyNE Resource (National Science Foundation ECCS-2025633), the IIN and Northwestern's MRSEC programme (National Science Foundation DMR-1720139). We thank C. Ballif and C. Wolf for assisting with module measurements. We also acknowledge O.A. Syzgantseva and M.A. Syzgantseva for suggestions on theoretical calculations and C. Igci and S. Dai for support with material synthesis and characterization. A.S.R.B. acknowledges support from King Abdullah University of Science and Technology through the Ibn Rushd Postdoctoral Fellowship Award.

Author contributions

C.L. conceived of the idea and proposed the experimental design. C.L. and Y.Y. performed the device fabrication and characterizations. A.L., Z.W., H.Z. and B.C. gave suggestions on the paper writing. J.D.F. and I.W.G. performed synthesis, physico-chemical analysis and crystallographic single-crystal analysis. C.B.M. performed DFT

calculation. R.P.R., K.R., R.S. and V.G. synthesized organic halides. B.D., Y.D., L.Z., Z.W. and X.Z. helped with the device fabrication. H.C., H.W. and A.S.R.B. helped with photoluminescence (PL) measurement. N.S. performed the GIWAXS measurement. K.R., P.J.D., M.G.K., M.K.N. and E.H.S. supervised the project. C.L. wrote the first draft of the paper. All the authors contributed to the revision and comments to the paper.

Competing interests
The authors declare no competing interests.

Additional information
Supplementary information The online version contains supplementary material available at https://doi.org/10.1038/s41560-025-01817-6.

Correspondence and requests for materials should be addressed to Kasparas Rakstys, Paul J. Dyson, Mercouri G. Kanatzidis, Edward H. Sargent or Mohammad K. Nazeeruddin.

Peer review information *Nature Energy* thanks Tongle Bu and the other, anonymous, reviewers for their contribution to the peer review of this work.

[1]Department of Chemistry, Northwestern University, Evanston, IL, USA. [2]Institute of Chemical Sciences and Engineering, École Polytechnique Fédérale de Lausanne (EPFL), Lausanne, Switzerland. [3]Department of Electrical and Computer Engineering, University of Toronto, Toronto, Ontario, Canada. [4]Department of Organic Chemistry, Kaunas University of Technology, Kaunas, Lithuania. [5]Department of Clinical Engineering, Toin University of Yokohama, Aoba-ku, Japan. [6]Department of Electrical and Computer Engineering, Northwestern University, Evanston, IL, USA. [7]Mechanical and Energy Engineering Department, College of Engineering, Imam Abdulrahman Bin Faisal University, Dammam, Saudi Arabia. ✉e-mail: kasparas.rakstys@ktu.lt; paul.dyson@epfl.ch; m-kanatzidis@northwestern.edu; ted.sargent@northwestern.edu; mdkhaja.nazeeruddin@epfl.ch

nature portfolio

Corresponding author(s): Ted Sargent

Solar Cells Reporting Summary

Nature Portfolio wishes to improve the reproducibility of the work that we publish. This form is intended for publication with all accepted papers reporting the characterization of photovoltaic devices and provides structure for consistency and transparency in reporting. Some list items might not apply to an individual manuscript, but all fields must be completed for clarity.

For further information on Nature Research policies, including our data availability policy, see Authors & Referees.

Experimental design

Please check the following details are reported in the manuscript, and provide a brief description or explanation where applicable.

1. Dimensions

Area of the tested solar cells	☒ Yes ☐ No	The aperture area for the solar cells was 0.05 cm2 (Methods). The aperture area for small and large modules was 17.2 cm2 and 30.74 cm2, respectively (Method-Characterization).
		Explain why this information is not reported/not relevant.
Method used to determine the device area	☒ Yes ☐ No	The aperture area of the solar cells was defined by an opaque metal mask with square aperture of area of 0.05 cm2 (Methods). The aperture area of small and large modules was defined by an opaque metal mask with rectangular apertures of 17.2 and 30.74 cm2, respectively (Method-Characterization).
		Explain why this information is not reported/not relevant.

2. Current-voltage characterization

Current density-voltage (J-V) plots in both forward and backward direction	☒ Yes ☐ No	See Fig. 5d,e and Supplementary Figure 28.
Voltage scan conditions	☒ Yes ☐ No	The scanning step was 20 and 50 mV for solar cells and modules, respectively. The scanning rate was 100 and 200 mV/s for solar cells and modules, respectively. (Method-Characterization).
		Explain why this information is not reported/not relevant.
Test environment	☒ Yes ☐ No	Current density (J)-voltage (V) characteristics of the devices were characterized at room temperature in air (Method-Characterization).
		Explain why this information is not reported/not relevant.
Protocol for preconditioning of the device before its characterization	☒ Yes ☐ No	No preconditioning of the device was applied before the measurement (Method-Characterization).
		Explain why this information is not reported/not relevant.
Stability of the J-V characteristic	☒ Yes ☐ No	See Figure 5h and Supplementary Figure 31 and 32.
		Explain why this information is not reported/not relevant.

3. Hysteresis or any other unusual behaviour

Description of the unusual behaviour observed during the characterization	☒ Yes ☐ No	The devices showed negligible hysteresis behaviors
		Explain why this information is not reported/not relevant.
Related experimental data	☒ Yes ☐ No	Figure 5d,e and Supplementary Figure 28
		Explain why this information is not reported/not relevant.

4. Efficiency

External quantum efficiency (EQE) or incident photons to current efficiency (IPCE)	☒ Yes ☐ No	See Supplementary Figure 27.
		Explain why this information is not reported/not relevant.

A comparison between the integrated response under the standard reference spectrum and the response measure under the simulator

☒ Yes
☐ No

The JSC obtained from the J-V characteristics was found to be consistent with the value integrated from the external quantum efficiency (EQE) spectrum. (Figure 5d and Supplementary Figure 27).

Explain why this information is not reported/not relevant.

For tandem solar cells, the bias illumination and bias voltage used for each subcell

☐ Yes
☒ No

Provide a description of the measurement conditions.

Explain why this information is not reported/not relevant.

5. Calibration

Light source and reference cell or sensor used for the characterization

☒ Yes
☐ No

Light source is a Xe arc lamp from a ScienceTech A1 Light Line Class AAA solar simulator. The reference solar cell is from Sciencetech (SCI-REF-Q) (Method-Characterization).

Explain why this information is not reported/not relevant.

Confirmation that the reference cell was calibrated and certified

☒ Yes
☐ No

The light intensity was calibrated by the reference solar cell (SCI-REF-Q) from Sciencetech (Method-Characterization).

Explain why this information is not reported/not relevant.

Calculation of spectral mismatch between the reference cell and the devices under test

☐ Yes
☒ No

Provide a value of the spectral mismatch and/or a description of how it has been taken into account in the measurements.

We rely on efficiency results verified by third parties.

6. Mask/aperture

Size of the mask/aperture used during testing

☒ Yes
☐ No

The active area of the solar cells was defined by an opaque metal mask with square aperture of the area of 0.05 cm2 (Methods). The aperture area of small and large modules was defined by an opaque metal mask with rectangular apertures of 17.2 and 30.74 cm2, respectively (Methods).

Explain why this information is not reported/not relevant.

Variation of the measured short-circuit current density with the mask/aperture area

☐ Yes
☒ No

Report the difference in the short-circuit current density values measured with the mask and aperture area.

We didn't measure the solar cells with apertures of different sizes.

7. Performance certification

Identity of the independent certification laboratory that confirmed the photovoltaic performance

☒ Yes
☐ No

The Photovoltaic Laboratory of the Institute of Micro Technique (IMT) in Switzerland.

Explain why this information is not reported/not relevant.

A copy of any certificate(s)

☒ Yes
☐ No

Supplementary Figure 26.

Explain why this information is not reported/not relevant.

8. Statistics

Number of solar cells tested

☒ Yes
☐ No

Eight devices for each condition were tested (Supplementary Figure 23).

Explain why this information is not reported/not relevant.

Statistical analysis of the device performance

☒ Yes
☐ No

Fig. 5c and Supplementary Figure 23.

Explain why this information is not reported/not relevant.

9. Long-term stability analysis

Type of analysis, bias conditions and environmental conditions

☒ Yes
☐ No

The maximum power point tracking (MPPT) measurement was conducted on the encapsulated devices under LED illumination (100 mW cm-2) at 85℃ with N2 flow. (See Figure 5h and Method-Characterization)

Explain why this information is not reported/not relevant.